Giant, 22, 2025, 100355

Full-length article

Miktoarm star polymers as templates for mesoporous phenolic materials: Enhancing microphase separation and expanding phase diagrams

Ting-Chih Chou, Shiao-Wei Kuo*

Department of Materials and Optoelectronic Science, Center of Crystal Research, National Sun Yat-Sen University, Kaohsiung 80424, Taiwan

Keywords: Miktoarm star polymers, Self-assembly, Mesoporous materials, Hydrogen bonding, Microphase separation

In the field of soft matter, designing different amphiphilic chemical structures could lead to the formation of ordered microphase-separated arrangements. Unlike linear block copolymers, miktoarm star polymers have been extensively utilized and inherently enhance the conformational asymmetry value (ε) in the microphase separation system through their branched chemical structure, allowing control over the interfacial curvature between microphase-separated domains and facilitating the formation of unique self-assembled structures, offering the potential to expand phase diagrams. In this study, we synthesized a common linear PEO-*b*-PCL diblock copolymer via ring-opening polymerization (ROP) and also prepared an AB_3-type block copolymer, PEO-*b*-PCL_3, by linking PEO to a branched PCL_3 block through a combination of ROP and click reactions with the similar volume fraction of PEO segment. Resol-type phenolic resin was synthesized by step-growth polymerization and used as the matrix, which was mixed with different weight fractions of linear PEO-*b*-PCL and miktoarm-type PEO-*b*-PCL_3 block copolymers as templates. FT-IR analysis of these blends at room temperature revealed that, under the similar volume fraction, the miktoarm-type star polymer forms the higher fraction of intermolecular hydrogen bonds with the phenolic resin in the PCL_3 block segment, and no crystallization was observed. Variable-temperature SAXS analysis demonstrated that upon thermal cross-linking, the blends exhibited improved stability and enhanced ordered microphase-separated structures. By heating to pyrolysis temperatures to remove the template, the resulting structures were characterized by using TEM and SAXS analyses. The systems constructed by two different templates creating mesoporous materials with different ordered structures such as lamellar, hexagonal columnar, spherical, BCC packing, and even the rare short-range order Frank-Kasper phase. Through phase diagram construction, we found that even with the similar weight fraction, the ordered mesoporous structures formed using the two different type of templates displayed significant differences. Additionally, the results indicated that when the branched segment of the miktoarm-type polymer is located at the core of the micelle, the interfacial curvature decreases. Overall, this study reveals the existence of the unique short-range order Frank-Kasper phase in systems with low χ values using wet-brush blending and validates the feasibility of employing miktoarm-type polymers as templates through analysis of molecular interaction and morphological characterization. This expands the phase diagram in the direction of tuning conformational asymmetry, providing a novel approach for designing innovative or specialized ordered mesoporous materials.

* Corresponding author.
E-mail address: kuosw@facutly.nsysu.edu.tw (S. Kuo).
Received 4 February 2025; Received in revised form 9 March 2025; Accepted 15 March 2025

 https://doi.org/10.1016/j.giant.2025.100355

1 Introduction

In the realm of soft matter, self-assembly has gained significant attention as a compelling research area, primarily due to its capacity to generate well-organized nanostructures with various functional properties. Amphiphilic molecules, consisting of both hydrophilic and hydrophobic segments, are especially proficient in forming a variety of hierarchical arrangements, including lamellae (LAM), double gyroid (DG), hexagonally packed cylinders (HEX), and body-centered cubic (BCC) packed spheres [1–4]. These structures exhibit significant potential for applications in drug delivery, fabrication of nanomaterials, biosensing, and energy storage, owing to their tunable size, morphology, and responsiveness to environmental changes [5–10]. The formation of self-assembled structures typically relies on several key parameters, including the molecular weight (N), volume fraction (f), and Flory-Huggins interaction parameter (χ).

Recently, there has been extensive research on modifying the self-assembly behavior of traditional block copolymers (BCPs) through molecular design and chemical synthesis [11–13]. One effective strategy is to control the conformational asymmetry (denoted as ε) between the blocks of the copolymer [14,15]. In general, using A and B blocks with a significant difference in statistical segment lengths (b_A and b_B) [16–18], or constructing asymmetric miktoarm star polymers (AB_n) where multiple B arms are attached to a common junction, has been proven to effectively enhance the value of ε in the system [19–23]. However, due to the inherent limitations of the material properties, increasing ε through the selection of block types has certain limits. In contrast, increasing the number of arms via molecular design is a more efficient method for raising the ε value and therefore has a greater level to control the conformational asymmetry. Previous studies have shown that branched block copolymers exhibit higher ε values while also enhancing interfacial curvature. This effect becomes more pronounced as the number of arms increases. Changes in interfacial area curvature tend to shift the phase transition boundaries in the phase diagram, expanding the regions where cylindrical and spherical structures occur. This can even stabilize unconventional packing structures, such as the Frank-Kasper phases. Bates et al. recently used poly(lactide) and poly(dodecyl acrylate) to enhance statistical segment length asymmetry and constructed AB_2 and AB_3 miktoarm star polymers using a sugar-based core. In this highly conformationally asymmetric system, they successfully formed the highly ordered Frank-Kasper A15 and σ phases [24]. Similarly, Sun et al. designed three different adaptors to synthesize PLA-*b*-$PDMS_n$ miktoarm star polymers with $n = 1$, 2, and 4. Their phase diagram illustrated how increasing the number of arms raises the system's conformational asymmetry, and they observed the formation of the Frank-Kasper A15 and σ phase when $n = 4$, validating the theoretical and simulation predictions that increasing ε facilitates the enhancement of interfacial area density at the same volume fraction [25].

The regulation of block copolymer/homopolymer blending systems through hydrogen bonding to fabricate ordered mesoporous phenolic/silica materials has garnered considerable attention over the past few decades [26–31]. Valkama and colleagues demonstrated that blending phenolic resin with HMTA curing agent and PS-*b*-P4VP resulted in the formation of an ordered hexagonally packed cylindrical mesoporous structure. This was attributed to the intermolecular hydrogen bonding between P4VP and phenolic resin under conditions where the PS weight fraction was 40 % [32]. In our previous work, we employed a linear diblock copolymer, poly(ethylene oxide-*b*-caprolactone) (PEO-*b*-PCL), with a fixed PEO molecular weight of 5,000 as a template in a phenolic resin system. By tuning competitive hydrogen bonding and compositional ratios under wet-brushing conditions, we achieved mesoporous carbon materials exhibiting DG, HPL, HPC, BCC, and Frank-Kasper phase structures [33–34]. Beyond controlling volume fractions through blending to regulate inorganic structural morphology, the macromolecule-guided strategy is an effective approach for fabricating highly ordered nanostructured ceramics. According to the review by Guo et al., this approach is categorized into two methods: the macromolecule-templated method, where amphiphilic macromolecules guide inorganic assembly, and the macromolecule-precursor method, where macromolecules containing non-volatile elements serve as single-source ceramic precursors. This strategy allows for precise structural control, broadening the potential applications of functional ceramics [35]. In addition to traditional diblock copolymers, triblock copolymers and hybrid block copolymers have also been explored for mesoporous material formation [36–39]. Vogt et al. used poly(ethylene oxide)-*b*-poly(ethyl acrylate)-*b*-polystyrene to generate high-porosity carbon films within a phenolic resin matrix [40]. To further increase the χ value and expand the phase diagram, we previously employed poly(methyl methacrylate)-*b*-poly(methacryloyl polyhedral oligomeric silsesquioxane) (POSS)blended with phenolic resin, controlling POSS content and phenolic resin concentration to produce ordered LAM, HPC, and spherical structures [41]. Hexagonal mesoporous silica materials were prepared from single-source giant surfactants composed of DPOSS heads and a PS tail. The pore size of silica materials expanded with increasing PS tail length, and the resulting material enhanced both the efficiency and stability of nanocatalysts [42]. Guo et al. fabricate the ordered mesoporous magnetic ceramics via pyrolysis of single-source self-assembled giant molecules composed of DPOSS, polystyrene, and ferrocene. The resulting materials exhibit a hexagonally ordered mesostructure, high surface area, uniform pore size, and ferromagnetic properties [43].

However, in the field of templating methods, while considerable progress has been made in manipulating self-assembly parameters such as polymerization degree (N), wet-brushing extent (α), and system interactions (χ), the influence and mechanism of controlling conformational asymmetry (ε) remains relatively underexplored. In this study, we successfully synthesized miktoarm star polymer PEO-*b*-PCL_3 with three arms using click chemistry, ensuring identical polydispersity between the branches. This allowed us to systematically investigate the impact of $\varepsilon > 1$ on self-assembled structures and compare these results with those obtained from linear diblock copolymer PEO-*b*-PCL with similar volume fractions. Through TEM and SAXS analysis, we characterized the resulting ordered mesoporous structures, demonstrating the distinct effects of increased conformational asymmetry. FT-IR spectroscopy further elucidated

the influence of the miktoarm architecture on competitive hydrogen bonding, aligning our findings with thermodynamic predictions. This work establishes the feasibility of employing miktoarm star polymers in conjunction with phenolic resin to produce ordered mesoporous materials. It also highlights that conformational asymmetry in the template plays a critical role in modulating interfacial curvature, shifting the volume fractions at which order-order phase transitions occur. Our findings underscore the importance of molecular design in governing the self-assembly behavior of block copolymer systems, providing offering new way to develop advanced mesoporous materials.

2 Experimental section

2.1 Materials

Tetrahydrofuran, hexane, diethyl ether, ethyl acetate, hydrochloric acid (ACS reagent, 37 %), 2-bromoethanol (95 %), dichloromethane (99.5 %) ε-caprolactone (99 %) and paraformaldehyde were purchased from Alfa Aesar. Sodium hydride (60 %, dispersion in paraffin liquid), Tin(II) 2-ethylhexanoate, sodium azide, copper(I) iodide (purum, ≥99.5 %), 4-pentynoic acid (95 %), 4-dimethylaminopyridine, diisopropylcarbodiimide, calcium hydride (95 %), and N,N′-Diisopropylcarbodiimide were purchased from Sigma-Aldrich. Acetic acid (Honeywell), N,N,N′,N′′,N′′-pentamethyldiethylenetriamine (99 %, TCI Chemicals), 2-(bromomethyl)-2-(hydroxymethyl)-1,3-propanediol (>99 %, TCI Chemicals), Sodium hydroxide (ACS reagent, ≥97.0 %, Showa), phenol detached crystal (>99 %, Fisher Scientific), calcium hydride (95 %, Acros), propargyl bromide (80 wt. % solution in toluene, stabilized, Thermo Scientific). Dimethylmethanamide (DMF), 2-bromoethanol, ε-caprolactone, toluene, dichloromethane were stirred with calcium hydride to dehydrate for 24 h, degassed to low pressure prior to distillation to sealed flask, and transfer by double-end solvent transfer infusion needle. Monomethoxy-poly(ethylene glycol) with a molecular weight of 5000 (PEO_{113}) was obtained from Fluka.

2.2 Synthesis of linear PEO-b-PCL diblock copolymer (Scheme S1)

PEO_{113} (5 g, 1 mmol) was added to 50 mL of anhydrous toluene under a nitrogen atmosphere. After heating the mixture to 140 °C, ε-caprolactone (10 g, 87.7 mmol) and Tin(II) 2-ethylhexanoate (40 mg, 0.1 mmol) were added and stirred for 24 h. Mixture was then degassed under low pressure to remove the toluene solvent and purified by dissolving it in THF and reprecipitating it in hexane three times. The white powder product was collected and dried in vacuo to acquire PEO_{113}-*b*-PCL_{130} (14.7 g,). Yield: 98 %. ^{1}H NMR ($CDCl_3$, 500 MHz, ppm, Figure S1): δ 4.10 - 4.03 (t, 176H), 3.64 (s, 454H), 2.33-2.27 (t, 176H), 1.69-1.60 (m, 352H), 1.43-1.34 (m, 176H).

2.3 The synthesis of 2-(bromomethyl)-2-((pent-4-ynoyloxy)methyl)propane-1,3-diyl bis(but-3-ynoate) (Scheme S2)

2-(Bromomethyl)-2-(hydroxymethyl)-1,3-propanediol (100 mg, 0.5 mmol), 4-pentynoic acid (160 mg, 1.6 mmol), and 4-dimethylaminopyridine (30 mg, 0.15 mmol) were dissolved in 30 mL of anhydrous DCM under a nitrogen atmosphere. The mixture was cooled to 0 °C. With stirring, N, N′-diisopropylcarbodiimide (0.348 mL, 2.25 mmol) was added dropwise to the reaction mixture through an addition tube. The mixture was then stirred at room temperature for 24 h. The precipitate was filtered out, and rotary evaporation was performed to obtain the crude product from the filtrate. Flash column chromatography filled with silica gel using DCM as the eluent was applied to purify the crude product. The 2-(bromomethyl)-2-((pent-4-ynoyloxy)methyl)propane-1,3-diyl bis(but-3-ynoate) as a linker was obtained as a transparent viscous liquid (210 mg). Yield: 80 %. ^{1}H NMR ($CDCl_3$, 500 MHz, ppm, Figure S2): δ 4.21 (s, 6H), 3.51 (s, 2H), 2.61-2.56 (m, 6H), 2.54-2.48 (m, 6H), 2.02-1.99 (m, 3H). FTIR (cm^{-1}, Figure S7(a)): 3290 (C≡C-H), 2121 (C≡C), and 1740 (C=O).

2.4 Synthesis of N_3-PCL (Scheme S3)

2-Bromoethanol (1.102 g, 8.82 mmol) was dissolved in 50 mL of anhydrous toluene under a nitrogen atmosphere. The solution was heated to 140 °C, after which ε-caprolactone (30.9 g, 0.271 mol) and Tin(II) 2-ethylhexanoate (40 mg, 0.1 mmol) were added and stirred for 24 hrs. The toluene solvent was then removed by degassing under low pressure. The resulting mixture was purified by dissolving it in THF and reprecipitating it in hexane three times. The final white powder product was collected and dried in *vacuo*, yielding Br-PCL (29.2 g). Yield: 91 %. ^{1}H NMR ($CDCl_3$, 500 MHz, ppm, Figure S3): δ 4.39 - 4.35 (t, 2H), 4.08-4.01 (t, 60H), 3.65-3.60 (t, 3H), 3.52-3.48 (t, 2H), 2.32-2.23 (t, 60H), 1.67-1.05 (m, 120H), 1.42-1.32 (m, 60H). FTIR (cm^{-1}, Figure S6(a)): 2945 (C-H stretching) and 1724 (crystalline C=O). Br-PCL (15 g, 4.28 mmol) and sodium azide (0.83 g, 12.84 mmol) were dissolved in anhydrous DMF. The mixture was heated to 70 °C and stirred overnight under a nitrogen atmosphere. The DMF solvent was then removed by applying a vacuum. The resulting product was dissolved in 200 mL of ethyl acetate (EA) and extracted with 200 mL of brine three times, followed by 100 mL of water twice. The organic layer was dried over $MgSO_4$. After removing the EA via rotary evaporation, the crude product was dissolved in DCM and reprecipitated into hexane three times. The final white powder product was collected and dried in *vacuo*, yielding N_3-PCL (13.8 g). Yield: 92 %. ^{1}H NMR ($CDCl_3$, 500 MHz, ppm, Figure S3): δ 4.27 - 4.22 (t, 2H), 4.08-4.01 (t, 60H), 3.65-3.60 (t, 3H), 3.52-3.48 (t, 2H), 2.32-2.23 (t, 60H), 1.67-1.05 (m, 120H), 1.42-1.32 (m, 60H). FTIR (cm^{-1}, Figure S6(b)): 2941 (C-H stretching), 2106 (N_3) and 1724 (crystalline C=O).

2.5 The synthesis of Br-PCL_3 (Scheme S4)

N_3-PCL (7.0 g, 2.059 mmol), 2-(bromomethyl)-2-((pent-4-ynoyloxy)methyl)propane-1,3-diyl bis(but-3-ynoate) (287.32 mg, 0.659 mmol), and CuI (0.4 eq per azide group) was dissolved by 50mL anhydrous DMF. The mixture was degassed by three freeze-pump-thaw cycles before the addition of PMDETA (1 eq per azide group) under the nitrogen environment. The mixture was heated to 70 °C and stirred for 12 h. Crude product was obtained via degassed the solution to low pressure to remove DMF. After that, THF was used to flash the crude product out of aluminum oxide column to remove the metal catalyst. The resulting product

was dissolve in DCM and reprecipitated in hexane three times, and collected in *vacuo* to obtain Br-PCL_3 as a white powder (5.2 g). Yield: 74 %. ^{1}H NMR ($CDCl_3$, 500 MHz, ppm, Figure S2): δ 7.39 (Azode, s, H), δ 4.08-4.01 (t, 180H), 2.32-2.23 (t, 180H), 1.67-1.05 (m, 360H), 1.42-1.32 (m, 180H). FTIR (cm^{-1}, Figure S6(c)): 2943 (C-H stretching), and 1724 (crystalline C=O).

2.6 The synthesis of N_3-PCL_3 (Scheme S5)

Br-PCL_3 (5 g, 4.28 mmol) and sodium azide (0.16 g, 2.45 mmol) were dissolved in anhydrous DMF. The mixture was heated to 75 °C and stirred overnight under a nitrogen atmosphere. The DMF solvent was then removed by applying a vacuum. The resulting product was dissolved in 200 mL of ethyl acetate (EA) and extracted with 200 mL of brine three times, followed by 100 mL of water twice. The organic layer was dried over $MgSO_4$. After removing the EA via rotary evaporation, the crude product was dissolved in DCM and reprecipitated into hexane three times. The final white powder product was collected and dried in vacuo, yielding N_3-PCL_3 (4.27 g). Yield: 85 %. ^{1}H NMR (CDCl3, 500 MHz, ppm, Figure S2): δ 7.39 (Azode, s, H), δ 4.08-4.01 (t, 180H), 2.32-2.23 (t, 180H), 1.67-1.05 (m, 360H), 1.42-1.32 (m, 180H). FTIR (cm^{-1}, Figure S6(d)): 2945 (C-H stretching), 2101 (N_3) and 1724 (crystalline C=O).

2.7 The synthesis of PEO-alkyne (Scheme S6)

PEO_{113} (5 g, 1 mmol) was dried by azeotropic distillation with toluene. Sodium hydride (115 mg, 8 mmol) was dissolved in 25 mL anhydrous THF and mixed with poly(ethylene oxide) methyl ether. Anhydrous propargyl bromide (0.606 mL, 8 mmol) was added dropwise into the mixture through syringe with the flask placed in an ice bath. After stirring for one day, THF and excess propargyl bromide was removed by rotary evaporation, the gel-liked mixture was extracted with 100 mL DCM for three times. The organic layer was dried by $MgSO_4$, and the resulting product was reprecipitated into ethyl ether three times. The obtained light brown powder was dried under vacuum to afford PEO-alkyne (4.7 g). Yield: 94 %. ^{1}H NMR ($CDCl_3$, 500 MHz, ppm, Figure S4): δ 4.20-4.16 (d, 2H), δ 3.65-3.59 (m, 452H), 2.39 (s, 1H). FTIR (cm^{-1}, Figure S7(b)): 3248 (C≡C-H), 2163 (C≡C), and 1104 (C-O-C).

2.8 The synthesis of PEO-*b*-PCL_3 (Scheme S7)

N_3-PCL_3 (1.8 g, 0.157 mmol), PEO-alkyne (0.8 g, 0.16 mmol), and CuI (0.4 eq per azide group) were dissolved in 50 mL of anhydrous DMF. The solution was degassed using three freeze-pump-thaw cycles before adding PMDETA (1 eq per azide group) under a nitrogen atmosphere. The mixture was heated to 75 °C and stirred for 18 hrs. The crude product was obtained by applying a vacuum to remove the DMF. THF was then used to flush the crude product through an aluminum oxide column to eliminate the metal catalyst. The resulting product was dissolved in DCM, reprecipitated in hexane three times, and dried in vacuum, yielding PEO-*b*-PCL_3 as a white powder (1.58 g). Yield: 61 %. ^{1}H NMR ($CDCl_3$, 500 MHz, ppm, Figure S5): δ 4.08-4.01 (t, 546H), δ 3.66-3.61 (m, 452H), δ 2.33-2.27 (t, 546H), δ 1.70-1.59 (m, 1092H), 1.44-1.32 (m, 452H). FTIR (cm^{-1}, Figure S7(c)): 2944 (C-H stretching), and 1724 (crystalline C=O).

2.9 The preparation of phenolic/EC and phenolic/EC_3 blends

Though the step growth polymerization of phenolic and paraformaldehyde under the alkaline environment, resole-type phenolic resin was synthesized (Scheme 1a) [44]. This simple thermosetting polymer was maintained in a pre-cured state (low cross-linked level) by controlling the polymerization time and served as the primary component (matrix) in the composite system. The linear diblock copolymer PEO-*b*-PCL (EC, Scheme 1b) and the miktoarm AB_3 block copolymer of PEO-*b*-PCL_3 (EC_3) was prepared by modifying the terminal functional groups of ε-caprolactone, using a click reaction to attach the intermediate linker and PEO block (Scheme 1c). Both block copolymers have similar volume fractions of PEO, with $f_{PEO,\,Linear}$ = 0.33 and $f_{PEO,\,Mik}$ = 0.30, respectively. To prepare the phenolic and block copolymer blends, THF was used as a neutral solvent. After thoroughly stirring the solution, it was poured into an aluminum pan. The solvent was then slowly evaporated in a convection oven set at 30 °C for 48 hrs to complete the evaporation-induced self-assembly (EISA) mechanism. Next, the pre-assembled blending samples were gradually heated to 150 °C, the cross-linking temperature of phenolic resin, and maintained at this temperature for 24 hrs. As the cross-linking degree of the phenolic resin domains increased, they shrunk and solidified, causing reaction-induced phase separation (RIPS) mechanism occurred within the blends.

2.10 Preparation of mesoporous phenolic resins

The cured blending samples were heated in a thermal convection high-temperature furnace to 400 °C, exceeding the thermal pyrolysis temperature of the PEO and PCL blocks, to remove the templates and create mesoporous structures within the phenolic resin domains (Scheme 1d). Finally, the bulk carbon material was ground into powder using a mortar and pestle. To maximize the degree of carbonization, the powdered material was heated to 800 °C in a tubular furnace under a nitrogen atmosphere, resulting in ordered mesoporous carbon material.

3 Results and discussion

Two amphiphilic block copolymers with different geometries but with the similar volume fractions were synthesized, both utilizing hydrophilic PEO and relative hydrophobic PCL as chemically incompatible blocks. PEO-*b*-PCL is a simple linear diblock copolymer, while PEO-*b*-PCL_3 is a miktoarm AB_3 block copolymer. Starting from ring-opening polymerization of the monomer, the halogen end-functional group in PCL was converted to N_3 via an S_N2 reaction (Scheme 2(a)). Through Steglich esterification, a linker possessing both a halogen functional group and three branched alkyne groups was successfully synthesized. This linker can undergo a click reaction with N_3-PCL, resulting in the formation of Br-PCL_3, where each arm has the same PDI (Scheme 2(c)). By replacing the Br atom in the linker with N_3 through another S_N2 reaction (Scheme 2(c)), the linker can be connected to alkyne-functionalized PEO (Scheme 2(b)) via a click reaction. This process ultimately yields the PEO-*b*-PCL_3 structure with three PCL branches on one side (Fig. 1(a) and Scheme 2(d)).

Fig. 1(b)-(d) show their corresponding FTIR, ^{1}H NMR and GPC analyses of N_3-PCL_3, alkyne-functionalized PEO, and PEO-*b*-PCL_3

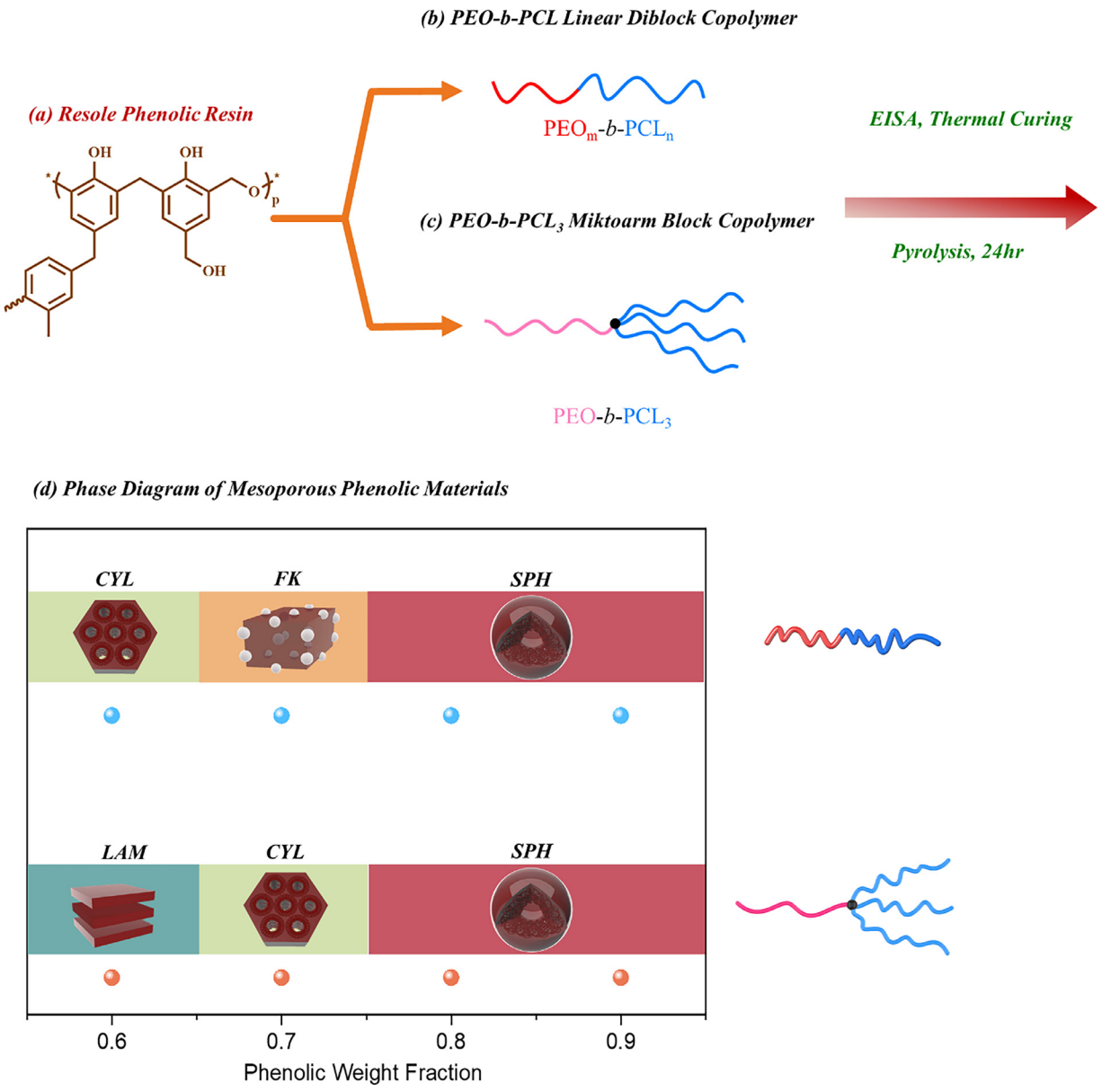

Scheme 1

The structure of (a) phenolic resin, (b) PEO-*b*-PCL linear diblock copolymer, (c) PEO-*b*-PCL miktoarm block copolymer, and (d) phase diagram of mesoporous phenolic resin templated by (b) and (c) block copolymers.

miktoarm block copolymer. The complete disappearance of the corresponding acetylene and azide units could be confirmed by FTIR analyses as displayed in Fig. 1(b). The azide unit observed at 2102 cm^{-1} of N_3-PCL_3 and the acetylene group of alkyne-functionalized PEO at 2164 cm^{-1} were completely disappeared in PEO-*b*-PCL_3 miktoarm block copolymer, suggesting that that both the acetylene and the azide functionalities reacted by the click reaction. The remained C=O group at 1724 cm^{-1} from N_3-PCL_3 and the C-O-C group at 1102 cm^{-1} from alkyne-functionalized PEO are both displayed in PEO-*b*-PCL_3 miktoarm block copolymer. The ^{1}H NMR peaks at 3.63 ppm corresponding to O-CH_2 (g) methylene units from PEO segment and CH_2 (e) methylene units from PCL segment, remained in PEO-*b*-PCL_3 miktoarm block copolymer as displayed in Fig. 1(c). GPC analyses suggested a narrow polydispersity of PEO-*b*-PCL_3 miktoarm block copolymer and it showed the relative lower retention time and no other peak from both N_3-PCL_3 and alkyne-functionalized PEO (Fig. 1(d)). All results based on FTIR, ^{1}H NMR and GPC analyses indicate the successfully synthesizing of PEO-*b*-PCL_3 miktoarm block copolymer. Furthermore, all molecular weight and polydispersity of each polymer used in this study were summarized in Table S1.

The pre-cured resole type phenolic resin was synthesized by controlled reaction time and temperature, in alkaline environment. Phenolic resin can form intermolecular hydrogen bonds with the ether groups of PEO or the C=O groups of PCL, as it is maintained in a pre-cured state. To ensure uniform mixing and the formation of an ordered self-assembled structure, we employed the common thermal treatment method for preparing ordered mesoporous materials through evaporation-

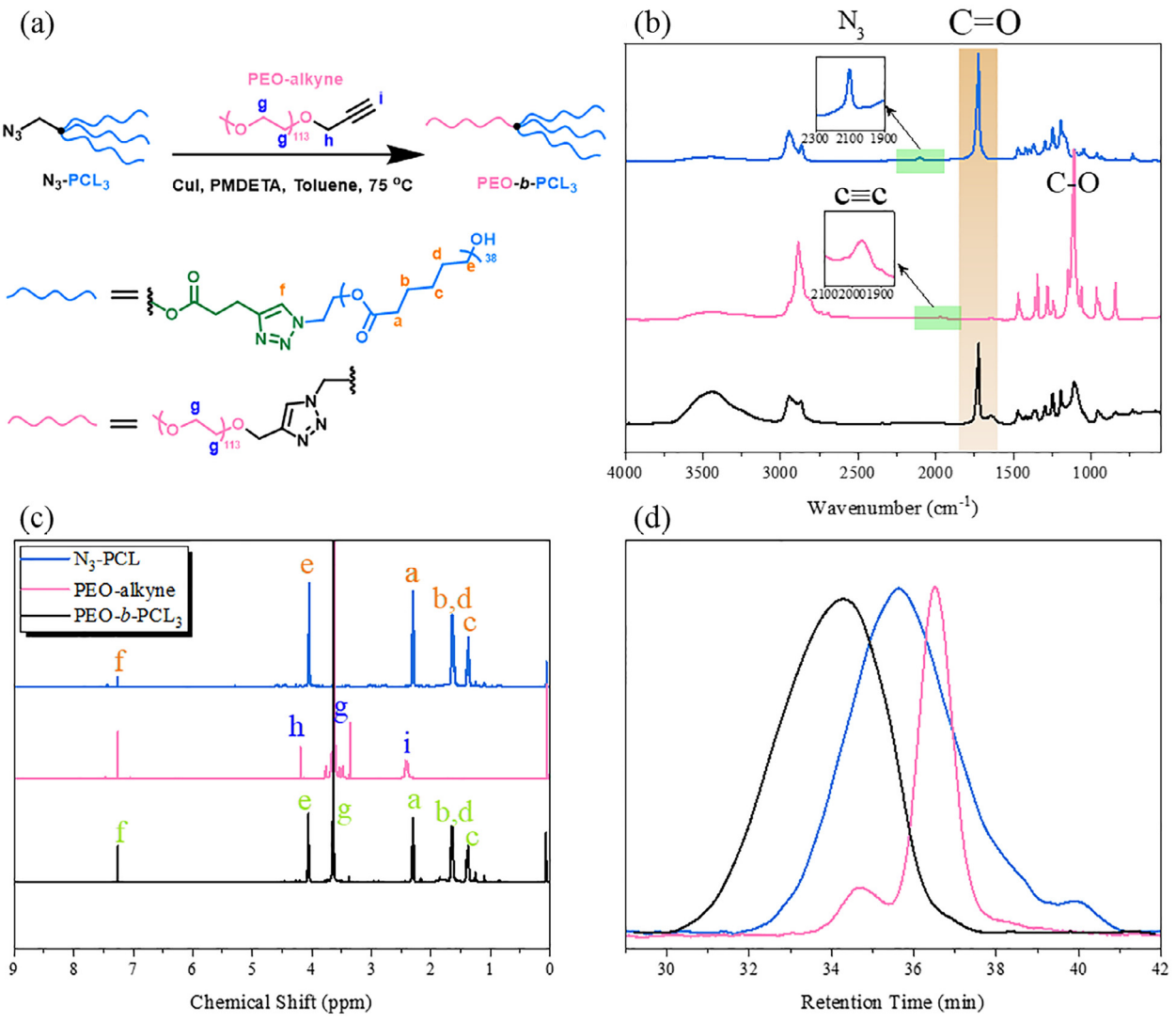

Fig. 1

(a) The synthesis of PEO-*b*-PCL miktoarm block copolymer through N_3-PCL_3 and PEO-alkyne by using click reaction and their corresponding (b) FTIR spectra, (c) 1H NMR spectra, and (d) GPC analyses.

induced self-assembly (EISA) mechanism. The phenolic/block copolymer blending samples were dissolved in a neutral solvent, and under controlled temperature conditions, the solvent slowly evaporated. As the solvent evaporated, the concentration of the solution increased, bringing the phenolic and block copolymer closer together and gradually strengthening the intermolecular hydrogen bonds. Under these conditions, to maintain the system's thermodynamic equilibrium, the amphiphilic templates PEO-*b*-PCL or PEO-*b*-PCL_3 can self-organized the phenolic into an ordered arrangement.

Firstly, for the room-temperature blending samples, we can use FT-IR analysis on samples with different volume fractions to observe how changes in Resole concentration affect the hydrogen bonding interactions with the template. We can also analyze the differences in interactions between the linear and miktoarm copolymers. Fig. S8 displays OH stretch region of phenolic groups for phenolic/EC and phenolic/EC_3 blending samples. We observe that as the phenolic concentration decreases, the sharp peak which represents the self-association hydrogen bonds initially at 3362 cm^{-1} gradually flattens out. This phenomenon is evident in both EC and EC_3 blends, suggesting the emergence of a new peak at a nearby wavenumber, leading to the overlapping of the two peaks and forming a plateau, especially noticeable when the phenolic concentration is 60 wt%. Through curve fitting simulations, we identify this new peak at 3285 cm^{-1}, which strengthens as the phenolic concentration decreases. According to previous studies [45–48], when phenolic acts as a hydrogen bond donor, both PEO and PCL serve as acceptors with the similar inter-association equilibrium constants (K_A). However, PEO has a slightly higher K_A value ($K_{A,PEO}$ = 264) compared to PCL ($K_{A,PCL}$ = 116) [46–48]. Therefore, for blends with lower donor concentrations, PEO preferentially forms intermolecular hydrogen bonds with all available phenolic donors. This results in the appearance of an OH stretch peak at 3285 cm^{-1}, representing the intermolecular hydrogen bonds between PEO and phenolic resin, forming the plateau at relative lower phenolic

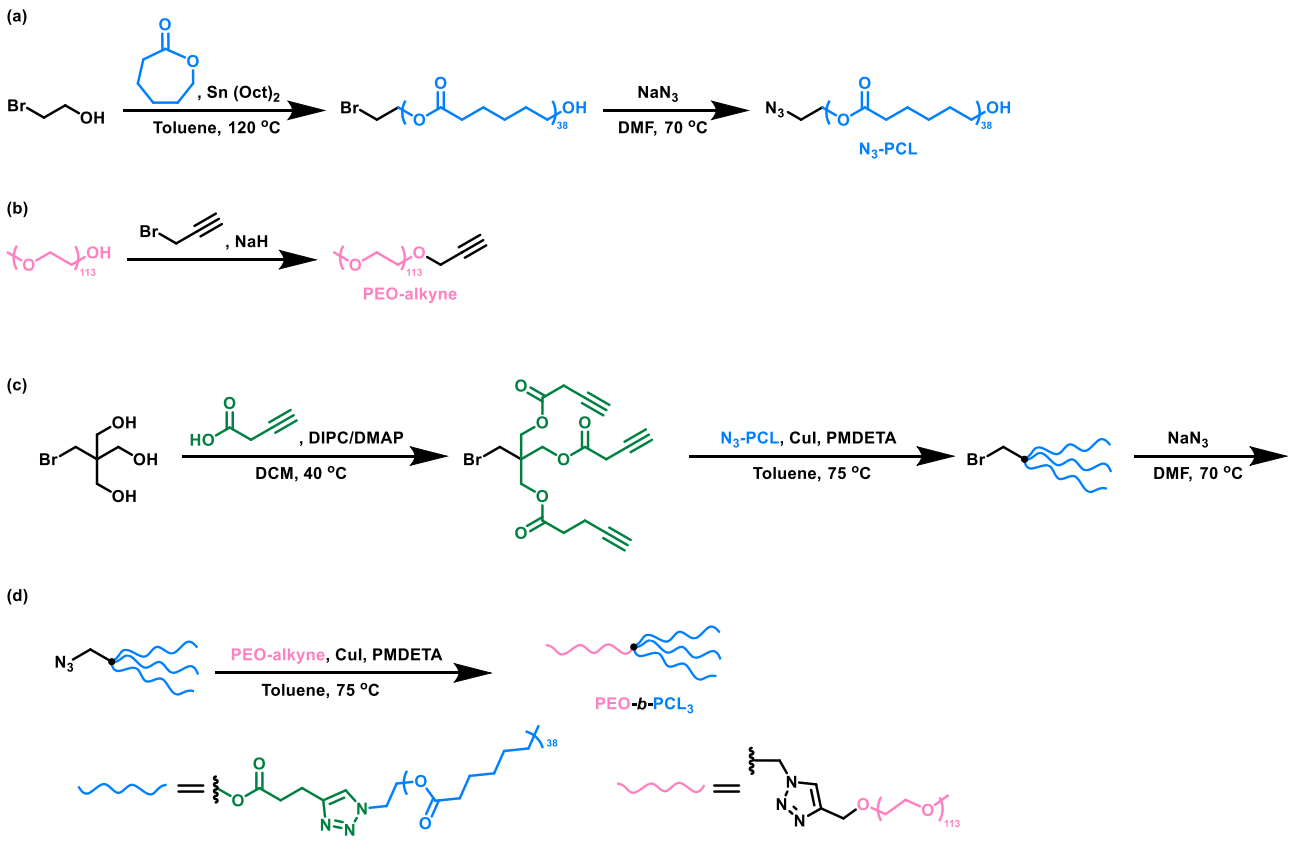

Scheme 2

The synthesis of (a) N_3-PCL, (b) PEO-alkyne, (c) N_3-PCL_3, and (d) PEO-*b*-PCL_3 block copolymer

concentration. Focusing on the carbonyl stretch region of PCL, we also observe significant changes in intermolecular interactions as the donor concentration in the blending samples varies. Fig. 2(a)-(d) illustrates the stretching peaks in the C=O region for the EC and EC_3 blends, with phenolic concentrations ranging from 90 to 60 wt%, along with their peak-fitting simulations. In both EC and EC_3 blends, the orange peaks at lower wavenumbers, representing hydrogen-bond interactions, weaken as the phenolic concentration decreases. PCL's lower K_A value means it has a lower priority for forming hydrogen bonds [46–48]. Consequently, at lower phenolic concentrations, the phenolic OH groups primarily form hydrogen bonds with PEO, leaving fewer phenolic OH groups available to interact with the PCL segments. This explains why the intensity of the C=O peaks affected by hydrogen bonding diminishes as the phenolic concentration decreased. Additionally, when comparing the C=O stretch behavior of templates with different chemical structures at the same phenolic concentration, several notable differences are observed. The C=O peak influenced by hydrogen bonding for the linear diblock copolymer EC appears at 1706 cm^{-1}, whereas for the miktoarm EC_3, this peak shifts to a higher wavenumber at 1712 cm^{-1}. Moreover, only the phenolic/EC blended samples exhibit a pink peak at 1724 cm^{-1}, representing the crystalline PCL characteristic peak. It is noteworthy that EC_3 exhibits more pronounced hydrogen bonding effects compared to EC at every blending ratio. We attribute this phenomenon to the differences in the degree of polymerization and the chemical structure of the PCL segments. Although EC and EC_3 have similar volume fractions, the miktoarm structure of EC_3 results in each branched PCL segment having a molecular weight approximately one-third that of the PCL in EC.

According to previous studies [46,47], longer polymer chains tend to self-coil more strongly. Thus, compared to the PCL chains in EC, which have a molecular weight close to 10,000 g/mol, the PCL segments in EC_3, with a significantly lower molecular weight of 3760 g/mol, exhibit reduced self-coiling. This makes them less prone to self-screening, allowing for greater intermolecular contact with phenolic OH groups, thereby enhancing hydrogen bonding in the PCL regions of EC_3. Furthermore, the branched geometry of the PCL in EC_3 creates a more spatially dispersed structure compared to the linear configuration of EC. This lower spatial hindrance at the molecular level provides phenolic chains with a more accessible environment, contributing to the higher fraction of hydrogen bonding interactions observed in EC_3, preventing the phenolic/EC_3 from crystallization. Figure S9 summarizes the variation trends in hydrogen bonding strength within the C=O region of phenolic/EC and phenolic/EC_3 blending samples as a function of different phenolic concentrations. The line graph clearly illustrates the relative fraction of hydrogen bonding in EC and EC3, as well as the competitive effects of hydrogen bonding induced by varying phenolic concentrations.

After undergoing the initial thermal treatment (EISA), we employed SAXS measurements to analyze the microphase

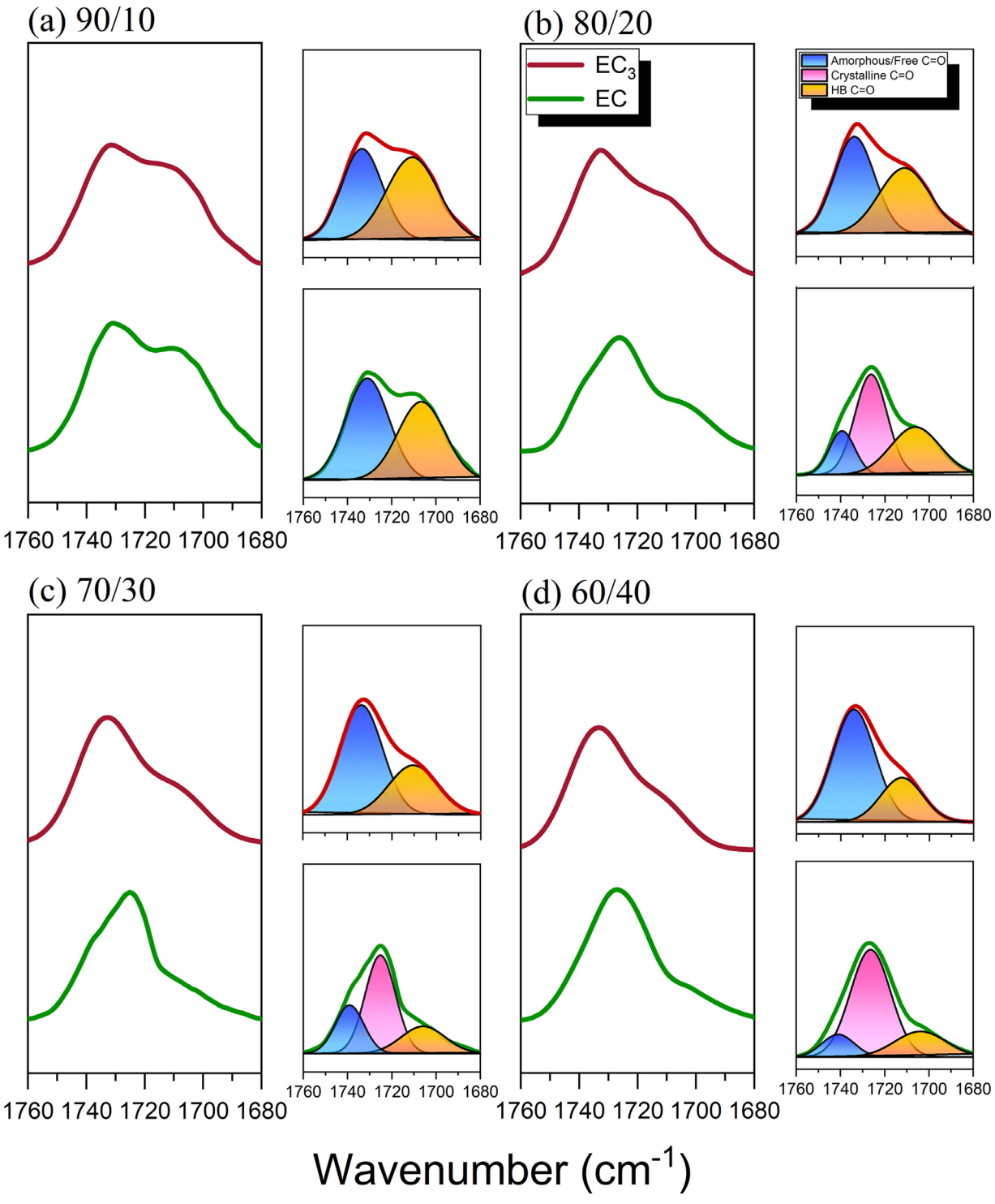

Fig. 2

FTIR spectra and their corresponding curve fitting results about C=O region of phenolic/EC and phenolic/EC_3 blends with various compositions of (a) 90/10, (b) 80/20, (c) 70/30, and (d) 60/40.

separation states of the microstructures in all samples. For the phenolic/EC blend samples, the 60 wt % phenolic resin exhibited a characteristic q-ratio of 1:$\sqrt{7}$, indicating a short-range order cylindrical structure with a domain size of 41.33 nm based on the Bragg equation, as shown in Fig. 3(a). For the samples with phenolic concentrations above 70 wt%, only a single first-order peak was observed, with domain sizes of 39.26, 38.31, and 34.78 nm, respectively, as illustrated in Fig. 3(b)-(d). The phenolic/EC_3 samples showed the similar behavior, with all blending ratios displaying only a first-order peak after EISA, and no other characteristic peaks were present. Using the q-values provided in Fig. 3(e)-(h), we calculated the domain sizes of the

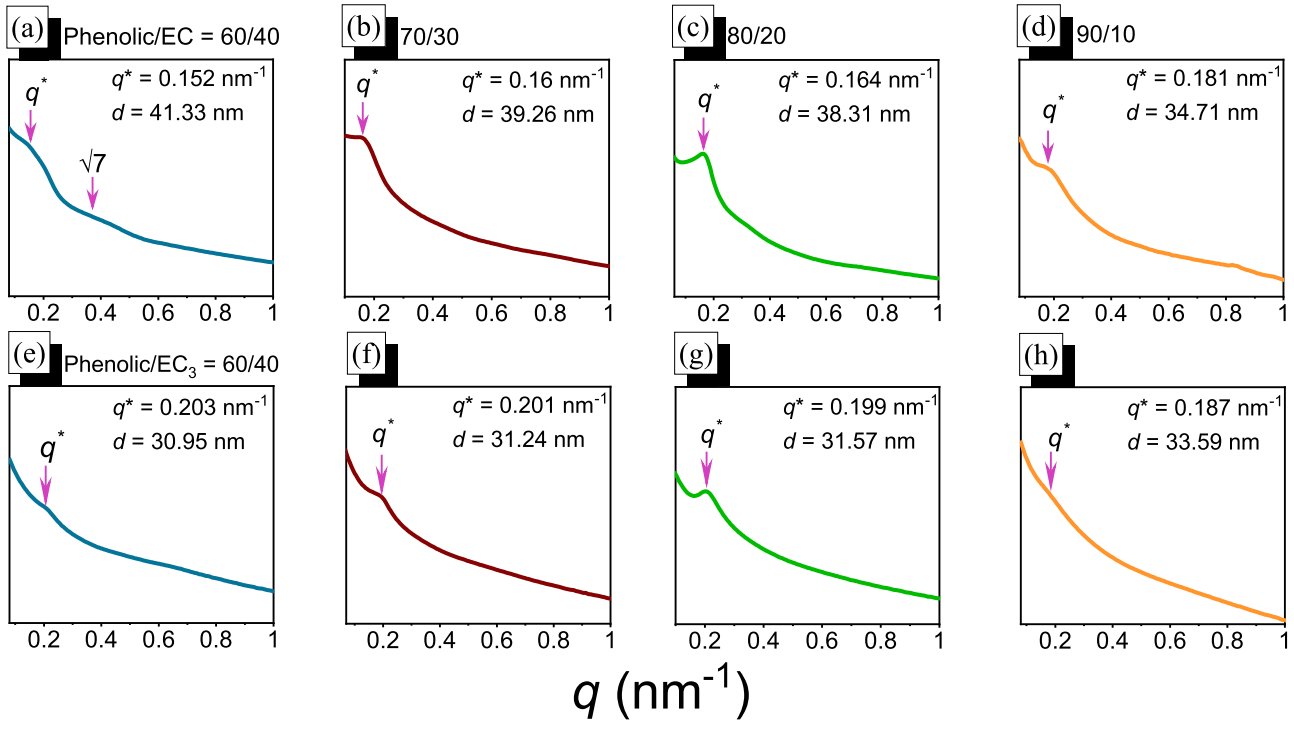

Fig. 3

SAXS analyses of phenolic/EC and phenolic/EC_3 blends at room temperature of (a, e) 60/40, (b, f) 70/30, (c, g) 80/20, and (d, h) 90/10, respectively.

microphase-separated structures for phenolic/EC_3 ratios ranging from 60/40 to 90/10, which were 30.95, 31.24, 31.57, and 33.59 nm, respectively. These data signify that, at fixed volume fractions, the linear template forms larger phase-separated structures.

We suggest that this is due to the miktoarm structure's branched architecture, which allows better utilization of space between and within PCL chains in the hydrophobic phase, resulting in more tightly packed chains and smaller domain sizes. Moreover, the SAXS profiles of both EC and EC_3 lack significant characteristic signals beyond the main peak, with some blending ratios exhibiting broad and poorly resolved main peaks. Here, we attribute this phenomenon to two possible reasons. First, the pre-cured phenolic resin has low mechanical strength and flexibility, providing less stability to the microphase-separated micelles [33,34,44,49]. Additionally, the strong crystallinity of PEO and PCL blocks, with crystallization temperatures close to room temperature, may disrupt the microphase-separated structures during the EISA process, reducing the orderliness of the material and leading to less distinct SAXS signals [34,44,49]. Although the hydrogen bonding between phenolic resin and the templates can partially inhibit crystallization, Fig. 2 shows that some blending ratios still exhibit crystalline signals from PCL that are not affected by hydrogen bonding, indirectly confirming that the order of the self-assembled system can indeed be disrupted by crystallization. Second, the low electron density contrast of the PEO and PCL blocks results in weak SAXS signals. Previous studies have shown that phenolic resins modified with POSS units, due to the contrast electron density and high Flory-Huggins interaction parameter (χ) value provided by inorganic silicon atoms, exhibited strong contrast even after blending with PEO-*b*-PCL templates, allowing for clear identification of the phase-separated structures [33,34,44,50]. In this study, the use of pure phenolic resin without any contrast-providing components may have resulted in poorly resolved SAXS profiles, making it difficult to determine the microphase-separated structures.

Variable temperature SAXS was employed to examine the microphase separation changes during the crosslinking process of the blends, with temperature increments of 30 °C from room temperature up to 180 °C, thereby simulating the thermal treatment environment of the samples. In the phenolic/EC combinations, SAXS patterns revealed that the *d*-spacing increased with rising temperature across all blend ratios (Fig. 4). For instance, in the phenolic/EC=60/40 blend, the *d*-spacing at room temperature was 35.69 nm. As the temperature increased, the *d*-spacing values at 60 °C, 90 °C, 120 °C, 150 °C, and 180 °C were 36.53 nm, 37.39 nm, 37.39 nm, 37.39 nm, and 38.31 nm, respectively, as depicted in Fig. 4(a). The crosslinking of phenolic resin leads to an increase in molecular weight and a concurrent microscopic volumetric shrinkage, resulting in an expansion of the internal space within the microphase-separated domains [33,34,44]. Additionally, in the phenolic/EC = 60/40 and 90/10 samples, a notable enhancement of the first-order peak or the appearance of a second characteristic peak was observed at 60 °C. This phenomenon is associated with the melting of PEO and PCL crystallites (T_m = 60 °C), which reduces the influence of crystallization on the microphase separation order. Starting from 60 °C, the increased degree of crosslinking enhances the overall mechanical strength of the system, enabling the microphase-separated structures to be maintained more stably. Moreover, the thermal crosslinking and melting of crystallites

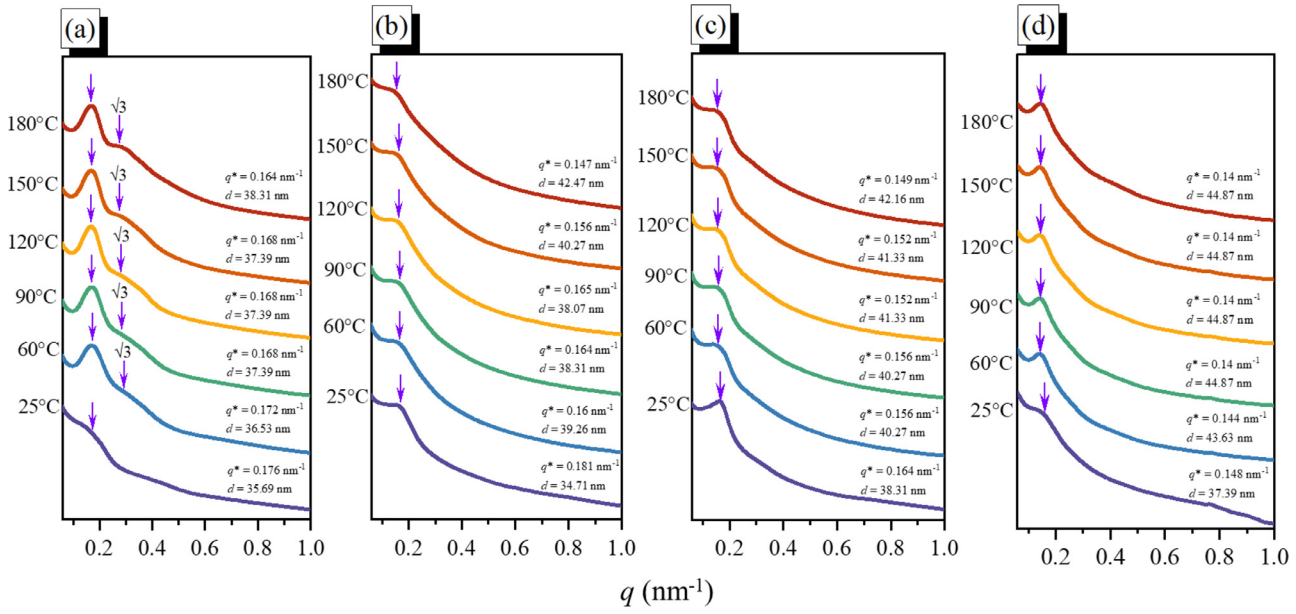

Fig. 4

SAXS analyses of phenolic/EC blends recorded at various temperatures of (a) 60/40, (b) 70/30, (c) 80/20, and (d) 90/10.

alter the interfacial energies at the microscopic level, leading to reaction-induced microphase separation (RIMPS). Consequently, this process results in an increased orderliness of the material [49,51–53].

Increasing the temperature of the phenolic/EC and phenolic/EC_3 blend samples to 400 °C results in the thermal decomposition of the polymer templates, leaving behind an ordered mesoporous carbon structure. The positions of the templates within the microphase-separated micelles become hollow due to pyrolysis, causing a partial loss of support in the phenolic domains and leading to slight deformation. Additionally, the relatively high temperature of 400 °C induces thermal deformation in the phenolic resin, contributing to the rearrangement of the microphase-separated order after template removal. Fig. 5 presents TEM images, SAXS patterns, and nitrogen adsorption/desorption isotherms of the mesoporous phenolic materials templated by EC with varying template contents. At a phenolic concentration of 60 wt%, a typical highly hexagonally packed cylindrical structure is observed, as indicated by the characteristic peak ratios of 1:$\sqrt{3}$:$\sqrt{4}$:$\sqrt{7}$ in the SAXS pattern (Fig. 5(a)), corroborated by the TEM projection (Fig. 5(e)). Increasing the phenolic concentration to 70 wt% reveals an intriguing microphase separation behavior in the mesoporous material. The TEM image in Fig. 5(f) shows an array of a single pore surrounded by multiple tightly packed pores, a feature of a Frank-Kasper phase. However, the SAXS analysis does not distinguish the scattering peaks of different planes; the SAXS curve in Fig. 5(b) only displays a primary peak and a plateau near $q/q^* = \sqrt{3}$, suggesting that the sample's order might be insufficient to yield high-resolution characteristic peaks. The superposition of multiple scattering peaks likely contributes to the formation of the plateau in the SAXS curve. Therefore, we infer that the sample possesses a short-range ordered Frank-Kasper Z phase based on its TEM projection behavior. For 80 wt% phenolic resin, the material continues to exhibit an array that resemble to Frank-Kasper phase, as shown in Fig. 5(g), with a plateau also appearing in the SAXS curve (Fig. 5(c)). Compared to phenolic/EC=70/30, the sample with phenoic/EC=80/20 exhibits lower order, leading us to categorize this mesoporous material as having a disordered spherical arrangement. Finally, when the phenolic concentration is increased to 90 wt%, the TEM image in Fig. 5(h) and the SAXS curve in Fig. 5(d), which features peak ratios of 1:$\sqrt{3}$:$\sqrt{7}$, confirm the formation of a body-centered cubic spherical packing. The N_2 adsorption/desorption analysis of the phenolic mesoporous materials is presented in Fig. 5(i)-(k). The phenolic/EC=60/40, 70/30, and 80/20 samples exhibit typical type IV(a) isotherms, with capillary condensation steps occurring from P/P_0 of 0.8 to 0.95. In the range of 0.4 to 0.9, H1-type hysteresis loops can be observed, indicating the presence of large-scale ordered cylindrical structures with mesoporous scales. The phenolic/EC=90/10 sample also displays a type IV(a) isotherm, with capillary condensation steps occurring between 0.95 and 1.0, and H1-type hysteresis loops appearing in the range of 0.5 to 1.0. Furthermore, pore size distribution analysis confirms that all samples fall within the mesoporous range, with pore diameters between 2 and 50 nm.

The microphase separation behavior of phenolic mesoporous materials from EC_3 template is displayed in Fig. 6. At a phenolic content of 60 wt%, the EC_3 template induces the formation of a lamellar structure, as suggested by the characteristic peak ratios of 1:2 in the SAXS profile (Fig. 6(a)) and the alternating black and gray stripes as displayed in TEM image (Fig. 6(e)). As the phenolic concentration increases to 70 wt%, the SAXS curve exhibits a low-order, small-range hexagonally packed cylindrical structure. Although peaks can be identified at the $q^*/q = 1$:$\sqrt{3}$:$\sqrt{7}$ positions, they are broad and weak in intensity. TEM analysis supports this result, as shown in (Fig. 6(b)). Unlike the conventional vertically close-packed cylindrical structure, the cylindrical mesopores

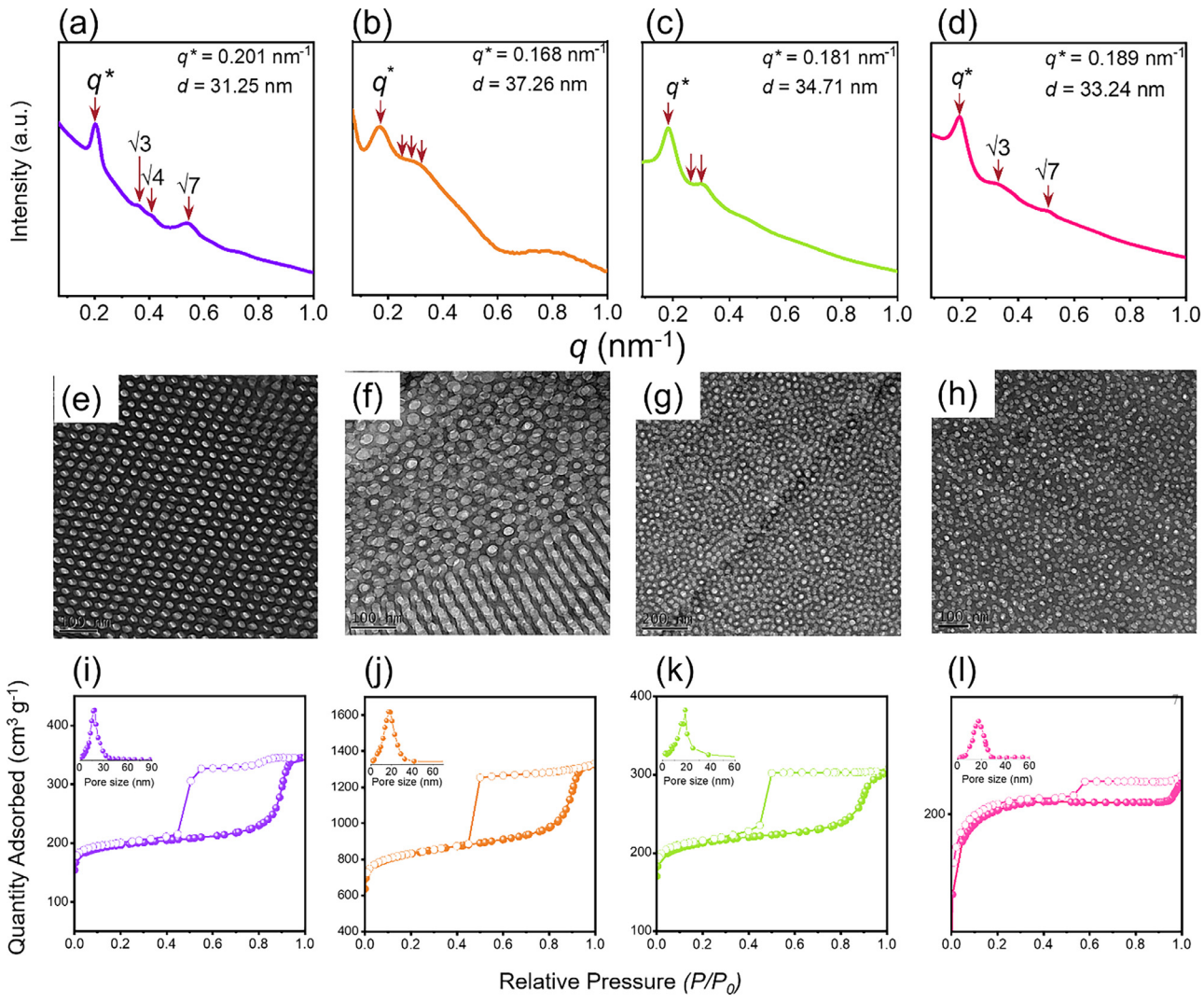

Fig. 5

SAXS analyses, TEM images, and N_2 adsorption/desorption isotherms of mesoporous phenolic materials templated from phenolic/EC blends of (a, e, i) 60/40, (b, f, j) 70/30, (c, g, k) 80/20, and (d, h, l) 90/10.

in the sample at this ratio exhibit a twisted morphology. Additionally, circular pores are observed, indicating that at this composition, the system is in a transition state of a spherical phase and cylindrical phase. This leads to the coexistence of distorted cylinders and circular pores in the TEM projection, ultimately resulting in a low degree of order at this specific blending ratio. With phenolic concentrations above 80 wt%, the samples exhibit spherical packing, as indicated by the presence of only primary peaks in the SAXS profiles (Fig. 6(c and d)), with the corresponding morphologies confirmed by TEM images (Fig. 6(g and h)). These phenolic mesoporous materials are characterized by IV(a) type isotherms, with hysteresis in the BET curves (Fig. 6(i)-(l)) indicating mesoporous structures. The capillary condensation steps occur at different P/P_0 values depending on the phenolic content: 0.5 to 0.85 from phenolic/EC_3 = 60/40 and 70/30 blends, 0.8 to nearly 1.0 from phenolic/EC_3 = 80/20 blend, and 0.7 to 1.0 from phenolic/EC_3 = 90/10 blend. The H4-type hysteresis loop observed during desorption in the phenolic/EC_3 = 60/40 sample suggests the presence of narrow slit-like pores, while the H5-type loop in the phenolic/EC_3 = 70/30 sample indicates partially blocked pores, consistent with the distorted cylindrical structures seen in the TEM images. The nearly horizontal desorption curve in the 0.5 to 1.0 of P/P_0 range from phenolic/EC_3 = 80/20 blend suggests an H2(a) type hysteresis loop, while the phenolic/EC_3 = 90/10 blend displays an H4-type loop within the 0.5 to 1.0 of P/P_0 range.

Table 1 summarizes all information of mesoporous materials derived from SAXS and BET analyses, with several key points worthy of discussion. First, the *d*-spacing of the mesoporous materials didn't exhibit a significant difference due to variations in the chemical structure of the template. In comparing pore volume and pore size, it is evident that the linear block copolymers display larger values than the miktoarm-type block copolymers. The branched structure of the PCL_3 block in EC_3 allows more efficient utilization of the core region's space, resulting in a smaller dimension at the microscopic level compared to the linear PCL, which is more difficult to fold, ultimately leading to a smaller pore size. Additionally, pore size characterization confirms

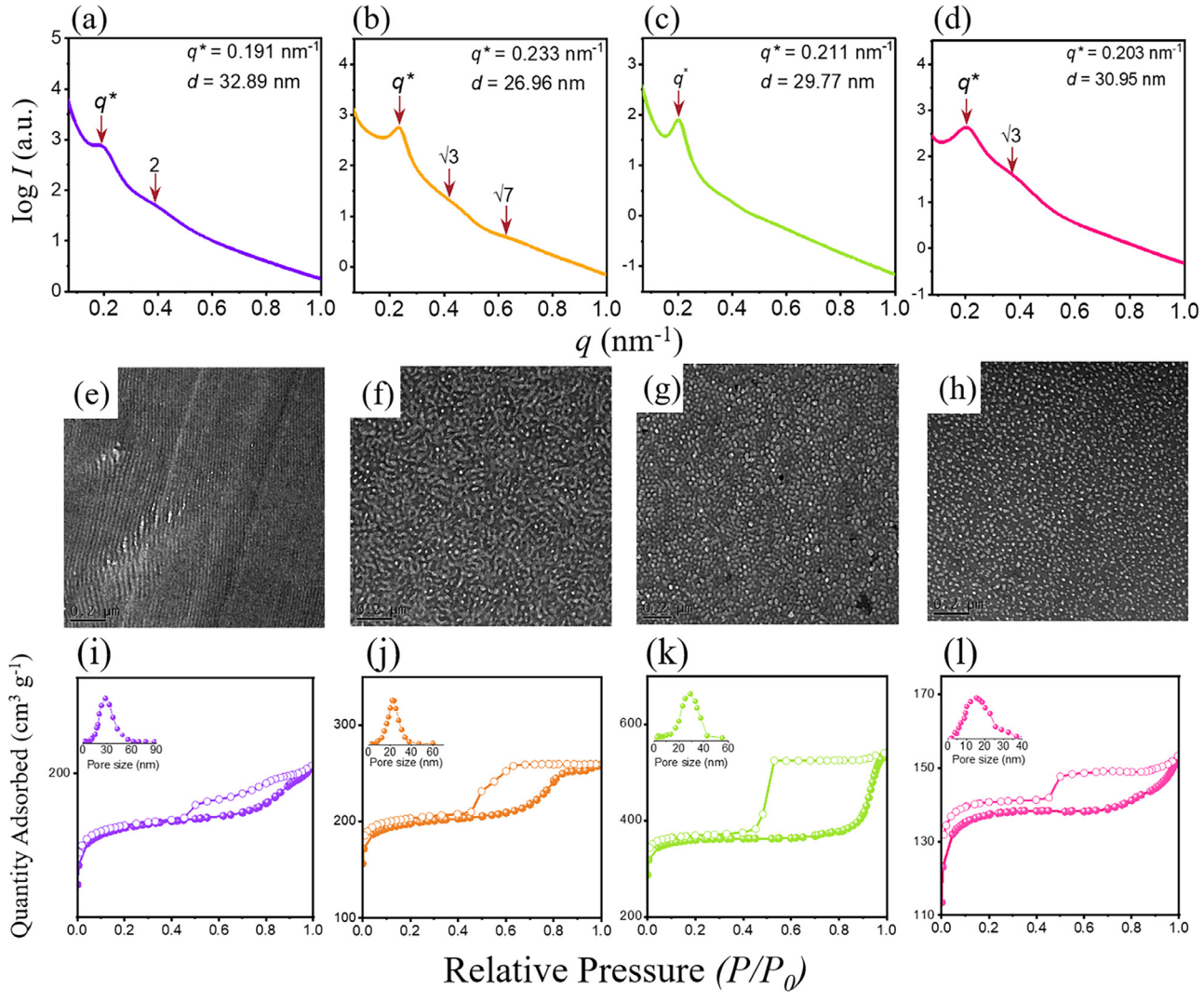

Fig. 6

SAXS analyses, TEM images, and N_2 adsorption/desorption isotherms of mesoporous phenolic materials templated from phenolic/EC_3 blends of (a, e, i) 60/40, (b, f, j) 70/30, (c, g, k) 80/20, and (d, h, l) 90/10.

Table 1

The SAXS and N_2 adsorption/desorption isotherms analyses of mesoporous phenolic materials templated by EC and EC_3 block copolymers

Samples	*d*-spacing (nm)[a]	S_{BET} (m^2/g)	S_M (m^2/g)	Pore Volume (cm^3/g)	Pore size (nm)[b]
Phenolic/EC = 6/4	31.25	611	470	0.045	14.2
Phenolic/EC_3 = 6/4	32.89	493	414	0.071	13.5
Phenolic/EC = 7/3	37.26	1588	1252	0.152	8.9
Phenolic/EC_3 = 7/3	26.96	610	500	0.076	5.4
Phenolic/EC = 8/2	34.71	659	515	0.071	9.3
Phenolic/EC_3 = 8/2	29.77	1102	968	0.061	7.1
Phenolic/EC = 9/1	33.24	614	538	0.065	13.1
Phenolic/EC_3 = 9/1	30.95	489	430	0.054	9.9

[a] The significant figures for *d*-spacing values calculated from the SAXS patterns are reported with two decimal places.
[b] The significant figures for pore size data obtained from BET analysis are presented with one decimal place.

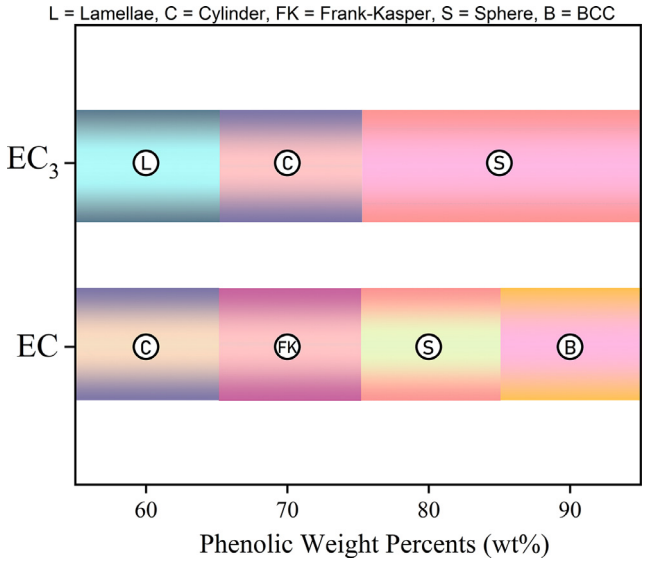

Fig. 7

Phase diagram of mesoporous phenolic materials templated by EC and EC_3 block copolymers in this study.

that the pore diameters of the porous materials prepared using both types of templates fall within the mesoporous range (2–50 nm). All samples in this study exhibit relatively high specific surface area values, indicating that these ordered mesopores are uniformly distributed throughout the material. Notably, the phenolic/EC = 70/30 blend sample demonstrates an exceptionally high specific surface area of 1588 m^2/g, along with the highest pore volume among all samples, reaching 0.152 cm^3/g.

Fig. 7 is the phase diagram of mesoporous phenolic materials templated from phenolic/EC and phenolic/EC_3 blends, we can clearly observe the microphase separation behavior of linear block copolymers compared to miktoarm-type block copolymers under varying blend ratios. It is evident that mesoporous materials templated by EC exhibit a greater diversity of microphase separation structures, a higher sensitivity to changes in volume fraction, and a higher degree of structural order than those templated by EC_3. Additionally, EC-templated samples generally exhibit higher interfacial curvature. At 60 % and 70 % phenolic weight fractions, higher curvature structures such as hexagonally packed cylinders and Frank-Kasper phases are formed, while the corresponding EC_3 samples produce structures with lower curvature, such as lamellae and cylindrical phases. These observations can be attributed to differences in the wet brush effect. The EC template contains a PCL block with a molecular weight of ca. 10,000 g/mol, whereas EC_3, due to its branched structure, consists of three PCL blocks, each with a molecular weight of ca. 3,500 g/mol. Since the phenolic resin has the same molecular weight in both systems, the wet brush parameter α, defined as $\alpha_{EC} = M_{n,PCL}/M_{n,phenolic}$ and $\alpha_{EC3} = M_{n,PCL3}/M_{n,phenolic}$, is approximately three times smaller for EC than for EC_3. A lower α value corresponds to a stronger wet brush effect, promoting better dispersion of phenolic homopolymer chains within the PCL domain. A higher degree of wet brushing allows the homopolymer to more effectively infiltrate the diblock copolymer region, reducing its free volume and restricting chain mobility. Thermodynamically, this leads to a significant loss in configurational entropy, which can dominate the system's free energy, as described by Gibbs free energy ($\Delta G = \Delta H - T\Delta S$). For example, in the case of the homopolymer phenolic resin, the EC diblock copolymer, with its higher molecular weight in the PCL segment, allows for better filling and dispersion within the diblock copolymer domain. As a result, the molecular chains in EC's PCL segment experience significantly greater restrictions on their mobility compared to EC_3, leading to a higher entropy loss. More importantly, when entropy loss surpasses a critical threshold, the system compensates by increasing interfacial curvature to achieve a new equilibrium [44,54–57]. Overall, when the same phenolic resin is blended with two different templates, the EC template, having a smaller molecular weight in the PCL segment, naturally results in a lower α value compared to EC_3, indicating a stronger wet-brush effect. According to the Gibbs free energy equation, a smaller α value leads to greater entropy loss. When this entropy loss surpasses the enthalpy threshold required to maintain the minimum free energy balance, the interfacial curvature increases, ultimately influencing the phase separation structure. Consequently, the lower α value of EC induces a stronger entropy loss and a greater increase in the interfacial curvature compared to EC_3 under the same blending ratio. Moreover, microphase separation occurs only when $\alpha < 1$, meaning that homopolymers can integrate into the microdomains of the diblock copolymer. Given that the phenolic resin has a molecular weight of 5,430 g/mol, EC_3's α exceeds 1, which should theoretically lead to macro-phase separation. However, the persistence of microphase separation in EC_3 can be attributed to hydrogen bonding constraints. As confirmed by FTIR analysis, the shorter PCL_3 chains allow for stronger hydrogen bonding with phenolic, while the branched structure enhances donor-acceptor interactions. This enables phenolic, which would otherwise be excluded, to enter the PCL_3 domain, mimicking the wet brush effect. Nevertheless, this mechanism is less effective in maintaining well-ordered structures, as reflected in the lower degree of order observed in EC_3-templated mesoporous materials via SAXS and TEM.

Previous studies have shown that branched chemical structures, due to their higher chain flexibility, are more prone to bending, making the interface more likely to curve toward the branched structure [19–23,58]. As illustrated in Scheme 2, in the phenolic/EC_3 system studied here, the phenolic resin primarily resides on the corona side during thermal processing due to the use of a template method. Moreover, due to competitive hydrogen bonding, the exterior corona region is occupied by the PEO block of the template, while the core region consists of the PCL_3 block. Hence, the branched sites are located in the micellar core in this system. We believe that the PCL_3 block, due to its branching effect, lowers the interfacial curvature, and coupled with the weaker wet brush effect, results in the formation of lamellar structures with zero interfacial curvature at a 60 % phenolic weight fraction.

In summary, using a linear EC diblock copolymer as a template and blending with phenolic at different weight fractions enables the formation of a series of ordered mesoporous materials with

various kinds of microphase-separated structures, including the rarely observed Frank-Kasper Z phase. The phase separation behavior varies significantly with volume fraction. The successful synthesis of EC_3 miktoarm block copolymers, and their ability to establish micro-phase separation structures confirmed by SAXS and TEM analysis, verifies that hydrogen bonding constraints allow PCL_3 to overcome molecular weight limitations from wet brushing. The phase diagram results demonstrate that using specialized miktoarm block copolymers as templates, even with branching at the micellar core, is a viable approach for producing ordered porous structures. This provides an alternative method for controlling interfacial curvature in microphase separation, offering valuable insights for expanding phase diagrams or fabricating mesoporous materials with unique phase-separated structures, such as Frank-Kasper phases or network structures.

4 Conclusions

In this study, we explored the effects and changes induced in a blend system when using a miktoarm star polymer as a template through various aspects of analysis. FT-IR analysis revealed that, even at the similar volume fraction, the miktoarm-type template can form higher fractdion of hydrogen bonds with phenolic resin, preventing crystallization in the PCL segment and retaining the competitive hydrogen bonding characteristics similar to linear PEO-*b*-PCL. The initial *d*-spacing was confirmed by SAXS, and temperature-dependent SAXS showed that thermal cross-linking and thermal curing of the phenolic matrix increased the order within the system, leading to an expansion of *d*-spacing due to the contraction of phenolic during cross-linking. The combined results from TEM, SAXS, and BET analysis enabled us to construct a phase diagram of the mesoporous materials after template removal. We confirmed that the linear template could produce mesoporous materials with CYL, SPH, BCC, and even the rare short-range Frank-Kasper phase self-assembled structures. In contrast, the miktoarm star polymer PEO-*b*-PCL_3 facilitated the formation of mesoporous materials with LAM, CYL, and SPH self-assembled structures. From a thermodynamic perspective, these differences in self-assembled structures for blends with the similar volume fraction, but different templates, can be explained. The linear PEO-*b*-PCL template, due to its higher PCL molecular weight, promotes wet-brush blending and thereby enhances the interfacial curvature, favoring the formation of self-assembled structures with higher interfacial curvature at the same volume fraction. Meanwhile, the miktoarm star polymer PEO-*b*-PCL_3, with shorter PCL chain lengths, would typically hinder the incorporation and dispersion of phenolic resin within its domain. However, the intermolecular hydrogen bonding overcomes this barrier, achieving an effect similar to wet-brushing, despite with a less pronounced increase in interfacial curvature compared to PEO-*b*-PCL. Additionally, the branched chemical structure located at the core position increases the conformational asymmetry in the core of the microphase-separated micelles, further reducing the interfacial curvature. Consequently, under the similar volume fraction, the mesoporous materials prepared using the miktoarm template tend to exhibit structures with lower interfacial curvature. In summary, this work demonstrates the feasibility of using miktoarm polymers as templates and highlights their differences from conventional linear polymers in terms of intermolecular interactions and self-assembled behavior. It provides a pathway for designing specific chemical structures to control the level of ε and α, thereby extending phase diagrams or creating unique mesoporous self-assembled structures.

Supplementary materials: Characterization methods, reaction schemce of phenolic resin, FITR, ^{1}H and ^{13}C NMR spectra of PEO-*b*-PCL and PEO-*b*-PCL_3 block copolymers, FTIR spectra analyses of phenolic/EC and phenolic/EC_3 blends.

Declaration of competing interest

The authors declare that they have no known competing financial interests or personal relationships that could have appeared to influence the work reported in this paper.

Data availability

No data was used for the research described in the article.

CRediT authorship contribution statement

Ting-Chih Chou: Writing – original draft, Formal analysis, Data curation. **Shiao-Wei Kuo:** Writing – review & editing, Supervision, Resources, Conceptualization.

Acknowledgements

This study was supported financially by the National Science and Technology Council, Taiwan, under contracts NSTC 113-2223-E-110-001- and 113-2221-E-110-012-MY3. The authors thank the staff at National Sun Yat-sen University for their assistance with the TEM (ID: EM022600) experiments.

Supplementary materials

Supplementary material associated with this article can be found, in the online version, at doi:10.1016/j.giant.2025.100355.

References

[1] L. Xiang, Q. Li, C. Li, Q. Yang, F. Xu, Y. Mai, Y. Block, Copolymer self-assembly directed synthesis of porous materials with ordered bicontinuous structures and their potential applications, Adv. Mater. 35 (2023) 2207684.

[2] J. Kim, H. Yun, Y.J. Lee, J. Lee, S.H. Kim, K.H. Ku, B.J. Jim, Photoswitchable surfactant-driven reversible shape- and color-changing block copolymer particles, J. Am. Chem. Soc. 143 (2023) 13333–13341.

[3] K.C. Yang, P. Puneet, P.T. Chiu, R.M. Ho, Well-ordered nanonetwork metamaterials from block copolymer templated syntheses, Acc. Chem. Res. 55 (2022) 2033–2042.

[4] S.W. Kuo, Construction archimedean tiling patterns based on soft materials from block copolymers and covalent organic frameworks, Giant 15 (2023) 100170.

[5] A. Rösler, G.W. Vandermeulen, H.A. Klok, Advanced drug delivery devices via self-assembly of amphiphilic block copolymers, Adv. Drug Deliv. Rev. 64 (2012) 270–279.

[6] M. Lazzari, M.A. López-Quintela, Block copolymers as a tool for nanomaterial fabrication, Adv. Mater. 15 (2003) 1583–1594.

[7] J.K. Kim, S.Y. Yang, Y. Lee, Y. Kim, Functional nanomaterials based on block copolymer self-assembly, Prog. Polym. Sci. 35 (2010) 1325–1349.

[8] C.E. Sing, J.W. Zwanikken, M.Olvera de, La Cruz, Electrostatic control of block copolymer morphology, Nature Mater 13 (2014) 694–698.

[9] J.G. Li, Y.F. Ho, M.M.M. Ahmed, H.C. Liang, S.W. Kuo, Mesoporous carbons templated by PEO-PCL block copolymers as electrode materials for supercapacitors, Chem. Eur. J. 25 (2019) 10456–10463.

[10] C. Li, Q. Li, Y.V. Kaneti, D. Hou, Y. Yamauchi, Y. Mai, Self-assembly of block copolymers towards mesoporous materials for energy storage and conversion systems, Chem. Soc. Rev. 49 (2020) 4681–4736.

[11] J.J. Shin, E.J. Kim, K.H. Ku, Y.J. Lee, C.J. Hawker, B.J. Kim, 100th anniversary of macromolecular science viewpoint: block copolymer particles: tuning shape, interfaces, and morphology, ACS Macro Lett. 9 (2020) 306–317.

[12] H. Dau, G.R. Jones, E. Tsogtgerel, D. Nguyen, A. Keyes, Y.S. Liu, H. Rauf, E. Ordonez, V. Puchelle, H. Basbug Alhan, Linear block copolymer synthesis, Chem. Rev. 122 (2022) 14471–14553.

[13] W. Li, C. Duan, A.C. Shi, Nonclassical spherical packing phases self-assembled from AB-type block copolymers, ACS Macro Lett 6 (2017) 1257–1262.

[14] F.S. Bates, G.H. Fredrickson, Conformational asymmetry and polymer-polymer thermodynamics, Macromolecules 27 (1994) 1065–1067.

[15] R.J. Sanchez-Leija, J.A. Mysona, J.J. de-Pablo, P.F. Nealey, Phase behavior and conformational asymmetry near the comb-to-bottlebrush transition in linear-brush block copolymers, Macromolecules 57 (2024) 2019–2029.

[16] M.W. Schulze, R.M. Lewis III, J.H. Lettow, R.J. Hickey, T.M. Gillard, M.A. Hillmyer, F.S. Bates, Conformational asymmetry and quasicrystal approximants in linear diblock copolymers, Phys. Rev. Lett. 118 (2017) 207801.

[17] S. Jeon, T. Jun, S. Jo, H. Ahn, S. Lee, B. Lee, D.Y. Ryu, Frank–kasper phases identified in PDMS-b-PTFEA copolymers with high conformational asymmetry, Macromol. Rapid Commun. 40 (2019) 1900259.

[18] K. Kim, A. Arora, R.M. Lewis III, M. Liu, W. Li, A.C. Shi, K.D. Dorfman, F.S. Bates, Origins of low-symmetry phases in asymmetric diblock copolymer melts, Proc. Natl. Acad. Sci. 115 (2018) 847–854.

[19] F.L. Beyer, S.P. Gido, G. Velis, N. Hadjichristidis, N.B. Tan, Morphological behavior of A5B miktoarm star block copolymers, Macromolecules 32 (1999) 6604–6607.

[20] N. Xie, W. Li, F. Qiu, A.C. Shi, σ phase formed in conformationally asymmetric AB-type block copolymers, ACS Macro Letters 3 (2014) 906–910.

[21] L. Yang, S. Hong, S.P. Gido, G. Velis, N. Hadjichristidis, I5S miktoarm star block copolymers: Packing constraints on morphology and discontinuous chevron tilt grain boundaries, Macromolecules 34 (2001) 9069–9073.

[22] C. Lee, S.P. Gido, M. Pitsikalis, J.W. Mays, N.B. Tan, S.F. Trevino, N. Hadjichristidis, Asymmetric single graft block copolymers: Effect of molecular architecture on morphology, Macromolecules 30 (1997) 3732–3738.

[23] D.J. Pochan, S.P. Gido, S. Pispas, J.W. Mays, A.J. Ryan, J.P.A. Fairclough, I.W. Hamley, N.J. Terrill, Morphologies of microphase-separated A2B simple graft copolymers, Macromolecules 29 (1996) 5091–5098.

[24] M.W. Bates, S.M. Barbon, A.E. Levi, R.M. Lewis III, H.K. Beech, K.M. Vonk, C. Zhang, G.H. Fredrickson, C.J. Hawker, C.M. Bates, Synthesis and self-assembly of ABn miktoarm star polymers, ACS Macro Letters 9 (2020) 396–403.

[25] Y. Sun, R. Tan, Z. Ma, Z. Gan, G. Li, D. Zhou, Y. Shao, W.B. Zhang, R. Zhang, X.H. Dong, Discrete block copolymers with diverse architectures: resolving complex spherical phases with one monomer resolution, ACS Cent. Sci. 6 (2020) 1386–1393.

[26] Y. Meng, D. Gu, F. Zhang, Y. Shi, L. Cheng, D. Feng, Z. Wu, Z. Chen, Y. Wan, A. Stein, A family of highly ordered mesoporous polymer resin and carbon structures from organic– organic self-assembly, Chem. Mater. 18 (2006) 4447–4464.

[27] L. Song, D. Feng, N.J. Fredin, K.G. Yager, R.L. Jones, Q. Wu, D. Zhao, B.D. Vogt, Challenges in fabrication of mesoporous carbon films with ordered cylindrical pores via phenolic oligomer self-assembly with triblock copolymers, ACS Nano 4 (2010) 189–198.

[28] A.F.M. EL-Mahdy, T.C. Yu, S.W. Kuo, Synthesis of multiple heteroatom–doped mesoporous carbon/silica composites for supercapacitors, Chem. Eng. J. 414 (2021) 128796.

[29] A.F.M. EL-Mahdy, T.E. Liu, S.W. Kuo, Direct synthesis of nitrogen-doped mesoporous carbons from triazine-functionalized resol for CO_2 uptake and highly efficient removal of dyes, J. Hazard. Mater. 391 (2020) 122163.

[30] M.G. Mohamed, E.C. Atayde Jr, B.M. Matsagar, J. Na, Y. Yamauchi, K.C.-W. Wu, S.W. Kuo, Construction hierarchically mesoporous/microporous materials based on block copolymer and covalent organic framework, J. Taiwan Inst. Chem. Eng. 112 (2020) 180–192.

[31] Y.C. Kao, Y.H. Ku, W.H. Su, M.G. Mohamed, S.W. Kuo, Microphase separation transformation in bio-based benzoxazine/phenolic/PEO-b-PCL diblock copolymer mixtures induced by transesterification reaction, Macromolecules 58 (2025) 585–600.

[32] S. Valkama, A. Nykänen, H. Kosonen, R. Ramani, F. Tuomisto, P. Engelhardt, G. ten Brinke, O. Ikkala, J. Ruokolainen, Hierarchical porosity in self-assembled polymers: post-modification of block copolymer–phenolic resin complexes by pyrolysis allows the control of micro-and mesoporosity, Adv. Funct. Mater. 17 (2007) 183–190.

[33] W.C. Chen, Y.T. Liu, S.W. Kuo, Mesoporous organic/inorganic hybrid materials with frank-kasper phases templated by an unusual linear symmetry diblock copolymer, Macromol. Rapid Commun. 42 (2021) 2100302.

[34] Y.C. Huang, W.C. Chen, S.W. Kuo, Mesoporous phenolic/poss hybrids induced by microphase separation arising from competitive hydrogen bonding interactions, Macromolecules 55 (2022) 8918–8930.

[35] Q.Y. Guo, B.X. Zhang, X. Feng, X.Y. Yan, Z. Su, S.Z. Cheng, K. Yue, Controlling the periodically ordered nanostructures in ceramics: a macromolecule-guided strategy, Macromol. Rapid Commun. 41 (2020) 1900534.

[36] D. Zhao, J. Feng, Q. Huo, N. Melosh, G.H. Fredrickson, B.F. Chmelka, G.D. Stucky, Triblock copolymer syntheses of mesoporous silica with periodic 50 to 300 angstrom pores, Science 279 (1998) 548–552.

[37] S.W. Kuo, Hydrogen bonding mediated self-assembled structures from block copolymer mixtures to mesoporous materials, Polym. Inter. 71 (2022) 393–410.

[38] T.W. Kim, F. Kleitz, B. Paul, R. Ryoo, MCM-48-like large mesoporous silicas with tailored pore structure: facile synthesis domain in a ternary triblock copolymer–butanol– water system, J. Am. Chem. Soc. 127 (2005) 7601–7610.

[39] W.T. Du, S.Y. Chen, S.W. Kuo, Mesoporous phenolic/carbon materials templated by CO2-based PEO-b-PCHC diblock copolymers through mediated competitive intermolecular hydrogen bonding interactions for CO2 capture, J. CO_2 Utilization 80 (2024) 102702.

[40] G. Deng, Z. Qiang, W. Lecorchick, K.A. Cavicchi, B.D. Vogt, Nanoporous nonwoven fibril-like morphology by cooperative self-assembly of poly (ethylene oxide)-block-poly (ethyl acrylate)-block-polystyrene and phenolic resin, Langmuir 30 (2014) 2530–2540.

[41] C.W. Chiou, Y.C. Lin, L. Wang, R. Maeda, T. Hayakawa, S.W. Kuo, Hydrogen bond interactions mediate hierarchical self-assembly of POSS-containing block copolymers blended with phenolic resin, Macromolecules 47 (2014) 8709–8721.

[42] Q.-Y. Guo, X.-Y. Yan, W. Zhang, X.-H. Li, Y. Xu, S. Dai, Y. Liu, B.-X. Zhang, X. Feng, J. Yin, Ordered mesoporous silica pyrolyzed from single-source self-assembled organic–inorganic giant surfactants, J. Am. Chem. Soc. 143 (2021) 12935–12942.

[43] Q.-Y. Guo, X.-H. Li, Y. Wu, X.-Y. Yan, Y. Liu, D. Han, B.-x. Zhang, X.-Y. Liu, H. Lei, Z. Su, Ordered mesoporous magnetic ceramics from single-source self-assembled ferrocene-functionalized giant molecules, CCS Chemistry 7 (2) (2025) 460–469.

[44] J.G. Li, P.Y. Lee, M.M. Ahmed, M.G. Mohamed, S.W. Kuo, Varying the hydrogen bonding strength in phenolic/PEO-b-PLA blends provides mesoporous carbons having large accessible pores suitable for energy storage, Macromol. Chem. Phys. 221 (2020) 2000040.

[45] T.C. Chou, S. Kuo, S.-W. Controllable wet-brush blending of linear diblock copolymers with phenolic/DDSQ Hybrids toward mesoporous structure phase diagram, Macromolecules 57 (2024) 5958–5970.

[46] S.W. Kuo, C.L. Lin, F.C. Chang, Phase behavior and hydrogen bonding in ternary polymer blends of phenolic resin/poly (ethylene oxide)/poly (ε-caprolactone), Macromolecules 35 (2002) 278–285.

[47] S.W. Kuo, Hydrogen-bonding in polymer blends, J. Polym. Res. 15 (2008) 459–486.

[48] J.G. Li, Y.D. Lin, S.W. Kuo, From microphase separation to self-organized mesoporous phenolic resin through competitive hydrogen bonding with double-crystalline diblock copolymers of Poly(ethylene oxide-b-ε-caprolactone), Macromolecules 44 (2011) 9295–9309.

[49] J.G. Li, W.C. Chu, U.S. Jeng, S.W. Kuo, Situ monitoring of the reaction-induced self-assembly of phenolic resin templated by diblock copolymers, Macromol. Chem. Phys. 214 (2013) 2115–2123.

[50] T.C. Chou, W.C. Chen, M.G. Mohamed, Y.C. Huang, S.W. Kuo, Organic-inorganic Phenolic/POSS hybrids provide highly ordered mesoporous structures templated by high thermal stability of PS-b-P4VP diblock copolymer, Chem. Eur. J. 29 (2023) e202300538.

[51] R. Yu, S. Zheng, X. Li, J. Wang, Reaction-induced microphase separation in epoxy thermosets containing block copolymers composed of polystyrene and poly (ε-caprolactone): influence of copolymer architectures on formation of nanophases, Macromolecules 45 (2012) 9155–9168.

[52] Z. Xu, S. Zheng, Reaction-induced microphase separation in epoxy thermosets containing poly (ε-caprolactone)-block-poly (n-butyl acrylate) diblock copolymer, Macromolecules 40 (2007) 2548–2558.

[53] C.F. Huang, W.H. Chen, J. Aimi, Y.S. Huang, S. Venkatesan, Y.W. Chiang, S.H. Huang, S.W. Kuo, T. Chen, Synthesis of well-defined PCL-b-PnBA-b-PMMA ABC-type triblock copolymers: toward the construction of nanostructures in epoxy thermosets, Polym. Chem. 9 (2018) 5644–5654.

[54] H. Tanaka, H. Hasegawa, T. Hashimoto, Ordered structure in mixtures of a block copolymer and homopolymers. 1. Solubilization of low molecular weight homopolymers, Macromolecules 24 (1991) 240–251.

[55] T. Hashimoto, H. Tanaka, H. Hasegawa, Ordered structure in mixtures of a block copolymer and homopolymers. 2. Effects of molecular weights of homopolymers, Macromolecules 23 (1990) 4378–4386.

[56] M.W. Matsen, Phase behavior of block copolymer/homopolymer blends, Macromolecules 28 (1995) 5765–5773.

[57] M.W. Matsen, Stabilizing new morphologies by blending homopolymer with block copolymer, Phys. Rev. Lett. 74 (1995) 4225.

[58] Y. Qiang, W. Li, A.C. Shi, Stabilizing phases of block copolymers with gigantic spheres via designed chain architectures, ACS Macro Lett 9 (2020) 668–673.